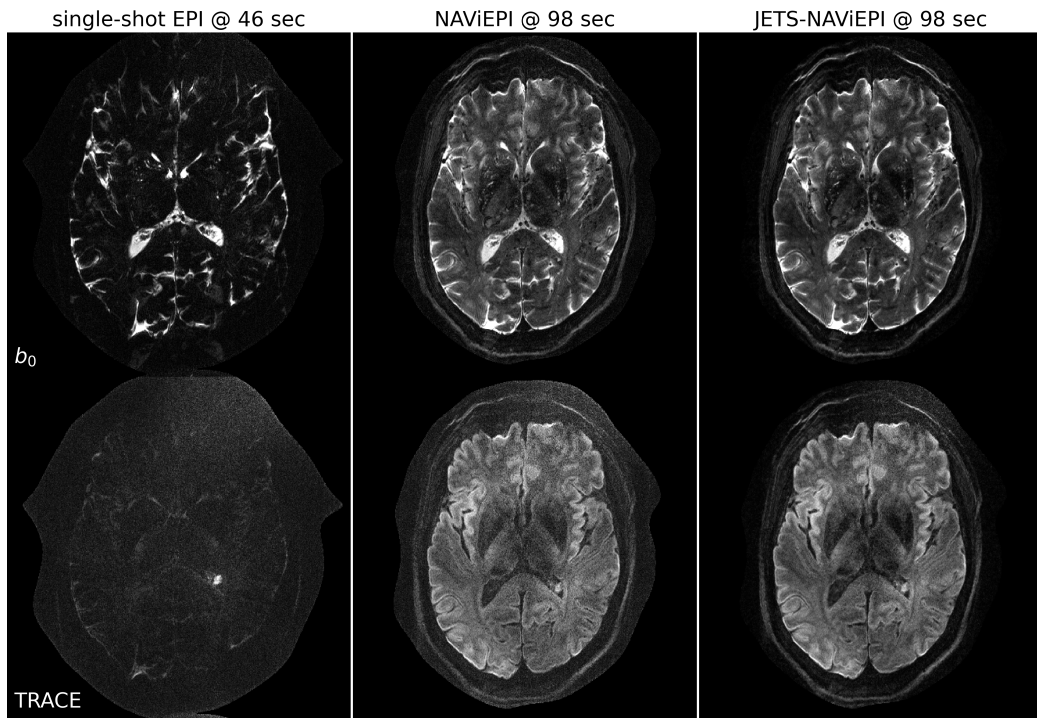


Graphical Abstract

Accelerated Diffusion Weighted Magnetic Resonance Imaging at 7 T: Joint Reconstruction for Shift-Encoded Navigator-based Interleaved Echo Planar Imaging (JETS-NAViEPI)

Zhengguo Tan, Patrick Alexander Liebig, Robin Martin Heidemann, Frederik Bernd Laun, Florian Knoll

3-scan trace acquisition with voxel size 0.5 X 0.5 X 2.0 mm³



Highlights

Accelerated Diffusion Weighted Magnetic Resonance Imaging at 7 T: Joint Reconstruction for Shift-Encoded Navigator-based Interleaved Echo Planar Imaging (JETS-NAViEPI)

Zhengguo Tan, Patrick Alexander Liebig, Robin Martin Heidemann, Frederik Bernd Laun, Florian Knoll

- Navigator-based interleaved EPI acquisition with minimal distortion mismatch between echoes
- Novel accelerated diffusion acquisition with shifted phase encoding among diffusion directions for complementary k - q -space sampling at 7 T
- Generalized joint k - q -slice diffusion-weighted image reconstruction with overlapping locally low-rank regularization
- Efficient simultaneous multi-slice (SMS) image reconstruction
- 3-scan trace acquisition with the voxel size $0.5 \times 0.5 \times 2.0 \text{ mm}^3$ and 60 slices at 1.5 min

Accelerated Diffusion Weighted Magnetic Resonance Imaging at 7 T: Joint Reconstruction for Shift-Encoded Navigator-based Interleaved Echo Planar Imaging (JETS-NAViEPI)

Zhengguo Tan^a, Patrick Alexander Liebig^b, Robin Martin Heidemann^b,
Frederik Bernd Laun^c, Florian Knoll^a

^a*Department Artificial Intelligence in Biomedical Engineering (AIBE),
Friedrich-Alexander University of Erlangen-Nuremberg, Erlangen, Germany*

^b*Siemens Healthcare GmbH, Erlangen, Germany*

^c*Institute of Radiology, University Hospital Erlangen, Friedrich-Alexander University of Erlangen-Nuremberg, Erlangen, Germany*

Abstract

The pursuit of high spatial-angular-temporal resolution for in vivo diffusion-weighted magnetic resonance imaging (DW-MRI) at ultra-high field strength (7 T and above) is important in understanding brain microstructure and function. Such pursuit, however, faces several technical challenges. First, increased off-resonance and shorter T_2 relaxation require faster echo train readouts. Second, existing high-resolution DW-MRI techniques usually employ in-plane fully-sampled multi-shot EPI, which not only prolongs the scan time but also induces a high specific absorption rate (SAR) at 7 T. To address these challenges, we develop in this work navigator-based interleaved EPI (NAViEPI) which enforces the same effective echo spacing (ESP) between the imaging and the navigator echo. First, NAViEPI renders no distortion mismatch between the two echoes, and thus simplifies shot-to-shot phase variation correction. Second, NAViEPI allows for a large number of shots

(e.g. > 4) with undersampled iEPI acquisition, thereby rendering clinically-feasible high-resolution sub-millimeter protocols. To retain signal-to-noise ratio (SNR) and to reduce undersampling artifacts, we developed a k_y -shift encoding among diffusion encodings to explore complementary k - q -space sampling. Moreover, we developed a novel joint reconstruction with overlapping locally low-rank regularization generalized to the multi-band multi-shot acquisition at 7 T (dubbed JETS-NAViEPI). Our method was demonstrated with experimental results covering 1 mm isotropic resolution multi b -value DWI and sub-millimeter in-plane resolution fast TRACE acquisition.

Keywords: Diffusion-weighted magnetic resonance imaging, Echo planar imaging, Navigator, Ultra-high field, Joint reconstruction, Low rank, Simultaneous multi slice

¹ **1. Introduction**

² Diffusion-weighted magnetic resonance imaging (DW-MRI) ([Le Bihan et al., 1986; Merboldt et al., 1985](#)) is a non-invasive modality that is sensi-
³ tive to the intravoxel Brownian motion of water molecules. DW-MRI forms
⁴ the basis for diffusion tensor imaging (DTI) ([Basser et al., 1994; Mori et al., 1999](#)) and high angular resolution diffusion imaging (HARDI) ([Tuch et al., 2002](#)), and has been widely used in acute brain ischemia diagnosis, in tumor
⁵ detection and staging, and in neuroscience ([Jones, 2010](#)).

⁶ For DW-MRI acquisition, the commonly used pulse sequence is single-
⁷ shot echo-planar imaging (SS-EPI) ([Mansfield, 1977](#)). SS-EPI is capable of
⁸ rapidly acquiring one DW image per radio-frequency excitation at the order
⁹ of 100 ms, and is thus motion robust. However, conventional SS-EPI, even
¹⁰ with three-fold accelerated acquisition ([Bammer et al., 2001](#)) using parallel
¹¹ imaging ([Roemer et al., 1990; Ra and Rim, 1993; Pruessmann et al., 1999](#);
¹² [Griswold et al., 2002](#)), still suffers from low spatial resolution and geometric
¹³ distortions.

¹⁴ In the quest for high spatial-angular-temporal-resolution and minimal-
¹⁵ geometry-distortion DW-MRI, tremendous efforts have been made. Tech-
¹⁶ niques for the correction of image distortions induced by off-resonances and
¹⁷ eddy currents have been developed ([Andersson et al., 2003](#)). Furthermore,
¹⁸ gSlider ([Setsompop et al., 2018](#)) with blipped-CAIPI ([Setsompop et al., 2012](#))
¹⁹ for simultaneous multi-slice (SMS) ([Maudsley, 1980; Breuer et al., 2005](#))
²⁰ was proposed to achieve high-resolution DW-MRI. Advanced pulse sequences
²¹ based on multi-shot EPI have also been developed, including but not limited
²² to interleaved EPI (iEPI) ([Butts et al., 1993](#)), PROPELLER ([Pipe et al., 2004](#)),

26 2002), and readout-segmented EPI (rsEPI) (Porter and Heidemann, 2009;
27 Heidemann et al., 2010).

28 Based on four-shot iEPI, multiplexed sensitivity encoding (MUSE) image
29 reconstruction achieved DW-MRI with a sub-millimeter in-plane resolution
30 and maximal b -value 800 s/mm^2 at 3 T (Chen et al., 2013). The four-shot
31 iEPI employed in MUSE acquired an in-plane fully-sampled k -space, except
32 partial Fourier. Every shot (segment), corresponding to four-fold under-
33 sampling, was then reconstructed via parallel imaging to obtain shot-to-shot
34 phase variation. This indicates that increasing the number of shots in MUSE
35 will result in higher undersampling per shot, and consequently, degrade shot
36 phase estimation (Wu and Miller, 2017).

37 Alternatively, navigator-based iEPI acquisition has been proposed (Jeong
38 et al., 2013; Dai et al., 2017, 2018). These proposals allow for a larger num-
39 ber of shots, and hence higher spatial resolution. However, due to the use of
40 different ESP between the imaging echo and the navigator echo, these pro-
41 posals suffered from geometric distortion mismatch between the two echoes
42 and thus required specific compensation methods. In contrast, rsEPI (Porter
43 and Heidemann, 2009; Heidemann et al., 2010) used the same readout seg-
44 ment for both echoes, and thus required no distortion correction of navigator
45 echoes.

46 Beyond the MUSE-type parallel imaging reconstruction, compressed sens-
47 ing (Lustig et al., 2007; Block et al., 2007) has been explored. For instance,
48 multi-shot reconstruction techniques based on structured low-rank matrix
49 completion (MUSSELS) (Mani et al., 2017; Bilgic et al., 2019) achieved 5-
50 shot DW-MRI with 9-fold undersampling per shot. Recently, JULEP (Dai

51 et al., 2023) incorporated explicit phase mapping into MUSSELS. These re-
52 construction techniques, i.e., MUSE, MUSSELS and JULEP, targeted the
53 reconstruction of one DW image from interleaved EPI acquisition, and did
54 not explore joint- k - q -space undersampling or reconstruction.

55 Joint- k - q -space undersampling can be achieved via proper regularization
56 along the diffusion encoding direction. Relevant examples are diffusion un-
57 dersampling with Gaussian process estimated reconstruction (DAGER) (Wu
58 et al., 2019) and magnitude-based spatial-angular locally low-rank regular-
59 ization (SPA-LLR) (Hu et al., 2020). However, DAGER addressed the re-
60 construction problem of single-shot EPI acquisition and SPA-LLR focused
61 on the reconstruction of single-band and fully-sampled iEPI acquisition.

62 In this work, we propose a Joint k - q -slice rEconsTruction framework
63 for Shift-encoded NAVigator-based interleaved EPI at 7 T (dubbed JETS-
64 NAViEPI). Our pulse sequence, NAViEPI, differs from most existing tech-
65 niques. First, NAViEPI builds upon interleaved EPI, thereby allowing for
66 fast and efficient k -space coverage. Second, inspired by rsEPI, NAViEPI en-
67 sures the same effective ESP between the imaging and the navigator echo,
68 thereby minimizing geometric distortion and allowing for the use of a larger
69 number of shots. NAViEPI essentially integrates the advantages of both iEPI
70 and rsEPI. Third, NAViEPI utilizes undersampled multi-shot iEPI, thereby
71 alleviating the SAR problem at 7 T. Fourth, NAViEPI shifts the k -space in-
72 plane sampling pattern along the phase encoding (k_y) direction. This shifting
73 creates complementary k - q -space sampling, which leads to the possibility of
74 our joint k - q -slice reconstruction. Specifically, we employ spatial-diffusion
75 overlapping LLR regularization to jointly reconstruct all diffusion encodings

⁷⁶ and multi-band slices. In vivo experiments at 7 T and comparisons with other
⁷⁷ techniques demonstrate the efficiency of our proposed method in achieving
⁷⁸ high spatial resolution DW-MRI at ultra-high field.

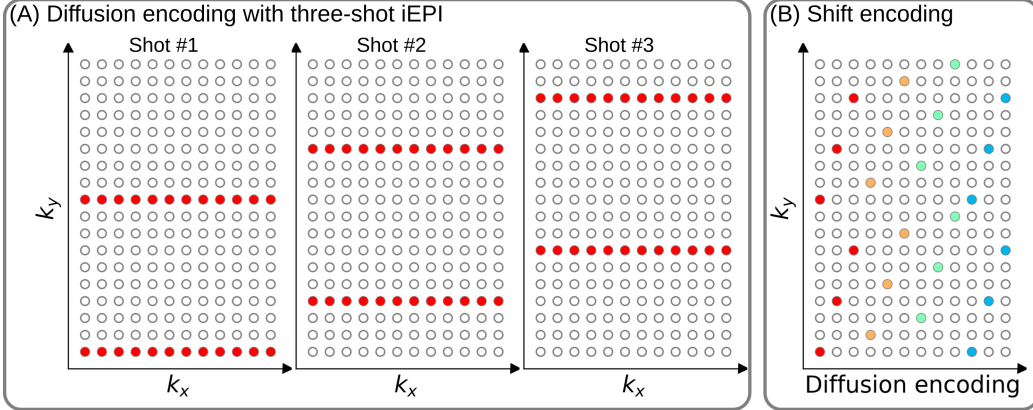


Figure 1: (A) An example DW-MRI acquisition with three-shot interleaved EPI acquisition. (B) The proposed k_y shifted diffusion encoding scheme. This example employs three shots per DW image. Therefore, every three columns have the same color.

79 2. Materials and methods

80 2.1. Multi-band shift-encoded iEPI acquisition

81 Fig. 1 (A) displays the diffusion-weighted image acquisition based on
 82 three-shot interleaved EPI with three-fold in-plane undersampling. Conven-
 83 tionally, such a sampling pattern is repeated for all diffusion directions. In
 84 contrast, we propose the k_y -shifted diffusion encoding, as shown in Fig. 1 (B).
 85 The interleaved EPI sampling pattern is shifted by one k_y line per diffusion
 86 direction, with the cycling period being the in-plane undersampling factor.

87 It is worth noting that, as shown in Fig. 1 (A), the undersampling factor
 88 of one segment is $R_{\text{in-plane}} \times N_{\text{shot}}$ (ignore multi-band undersampling here),
 89 yielding nine-fold in-plane undersampling in this example. In other words,
 90 the undersampling factor per segment linearly scales up with the number
 91 of shots. Consequently, conventional self-gating reconstruction techniques,
 92 e.g. MUSE, suffer from degraded shot-to-shot phase estimation, which in

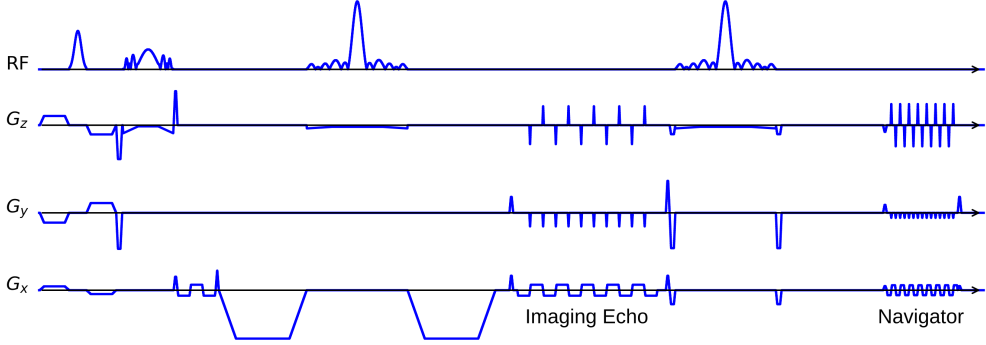


Figure 2: The NAViEPI sequence diagram. SMS is utilized for the acquisition of both imaging and navigator echoes. While the acceleration factor per navigator is the same as listed in Table 1, the acceleration factor per imaging echo is in addition linearly scaled by the number of shots.

93 turn limits the number of shots and spatial resolution.

94 *2.2. NAViEPI: Navigator-based iEPI with consistent effective ESP between
95 the imaging and the navigator echo - where iEPI meets rsEPI*

96 Instead of the self-gated MUSE with in-plane fully-sampled iEPI and
97 a limited number of shots, We propose NAVigator-based interleaved EPI
98 (NAViEPI), as illustrated in Fig. 2. Inspired by rsEPI (Porter and Hei-
99 demann, 2009), NAViEPI enforces a consistent effective ESP between the
100 imaging and the navigator echo, thereby minimizing distortion mismatch
101 between the two echoes.

102 Since one imaging echo presents one segment in multi-shot EPI acquisi-
103 tion, its effective ESP is defined as

$$\text{ESP}_{\text{eff}} = \frac{\text{ESP}}{R_{\text{in-plane}} \times N_{\text{shot}}} \quad (1)$$

104 Here, a larger number of shots (segments) increases the undersampling factor
105 per segment (see Fig. 1), but decreases the effective ESP. Since the navigator

106 echo is acquired for each segment, its in-plane undersampling factor equals
107 $R_{\text{in-plane}}$. Therefore, the effective ESP of the navigator echo must match that
108 of the imaging echo, as given in Eq. (1). With a matching effective ESP, the
109 base resolution of the navigator echo can then be determined.

110 *2.3. In vivo acquisition protocols*

111 We implemented multiple in-vivo acquisition protocols at a clinical 7 T
112 MR system (MAGNETOM Terra, Siemens Healthineers, Erlangen, Ger-
113 many) equipped with a 32-channel head coil (Nova Medical, Wilmington,
114 MA, USA) and the XR-gradient system (maximum gradient strength 80 mT/m
115 with a peak slew rate of 200 T/m/s). To calibrate coil sensitivity maps, refer-
116 ence scans employed a gradient-echo (GRE) sequence. Spectral fat saturation
117 and mono-polar diffusion-encoding gradients were used. The phase-encoding
118 direction was selected as anterior-to-posterior.

Table 1: NAViEPI acquisition protocols

Protocol	1.0 mm isotropic		sub-millimeter	
	#1	#2	#3	#4
Diffusion mode	MDDW ⁽¹⁾		3-scan trace	
Diffusion scheme	monopolar			
Diffusion direction	20	114	3	
<i>b</i> -value (s/mm ²)	1000	3-shell ⁽²⁾	1000	
<i>b</i> ₀	0	12	1	
FOV (mm ²)	200	214	220	
In-plane resolution (mm ²)	1.0		0.5	
Slice thickness (mm)	1.0		2.0	
Slices	141	114	60	
Navigator	No	No	Yes	No
Shots	4	2	5	1
TR (ms)	7700	5200	4400	8000
TEs (ms)	67	66	58/95.1	143
ESP (ms)	1.02	0.81	1.52	1.48
Bandwidth (Hz/Pixel)	1086	1460	758	
Partial Fourier			6/8	
Acceleration ⁽³⁾	1 × 3	3 × 3	3 × 2	
TA (min) ⁽⁴⁾	10 : 42	22 : 25	1 : 38	0 : 46

⁽¹⁾ MDDW: Multi-direction diffusion weighting;

⁽²⁾ 3-shell: 20, 30, and 64 directions with *b*-values of 1000, 2000, and 3000 s/mm², respectively;

⁽³⁾ Acceleration: Both in-plane and slice undersampling can be employed, denoted as (*R*_{in-plane} × *R*_{slice});

⁽⁴⁾ TA: Total acquisition time.

120 This study was approved by the local ethics committee. Three volunteers
121 with informed consent obtained before scanning participated in this
122 study. Detailed acquisition protocols are listed in Table 1. In the spirit of re-
123 producible research, another volunteer with informed consent was recruited
124 for the scan of all acquisition protocols, and the results were displayed in
125 Supplementary Information.

126 *2.3.1. 20-diffusion-direction acquisition at 1 mm isotropic resolution*

127 As listed in Table 1, Protocol #1 with four-shot iEPI and without in-
128 plane undersampling was implemented. This protocol represents the acquisi-
129 tion scheme employed in many existing multi-shot reconstruction techniques,
130 (e.g., MUSE, SPA-LLR, and JULEP). The acquired data from this protocol
131 served as ground truth. Different reconstruction methods, specifically JETS,
132 MUSE, and JULEP were compared. We compared with JULEP instead of
133 MUSSELS, because JULEP uses not only structured low-rank constraints
134 but also explicit phase mapping.

135 We then retrospectively reduced the four-shot data to only one shot per
136 diffusion encoding without and with the proposed k_y shifting to simulate
137 four-fold in-plane undersampling. JETS reconstruction was performed on
138 the fully-sampled data and the retrospectively undersampled data to validate
139 the proposed k_y -shifted acquisition.

140 *2.3.2. Three-shell acquisition at 1 mm isotropic resolution*

141 Protocol #2 in Table 1 was implemented for multi-shell diffusion tensor
142 imaging (DTI) (Basser et al., 1994). We acquired a total of 114 diffusion
143 directions, whereas b_0 measurements were interspersed every ten diffusion

₁₄₄ directions. This protocol was used to demonstrate the capability of JETS
₁₄₅ in achieving high spatial-angular-temporal resolution.

₁₄₆ *2.3.3. 3-scan trace acquisition at $0.5 \times 0.5 \times 2.0 \text{ mm}^3$ voxel size*

₁₄₇ As listed in Table 1, Protocol #3 was implemented based on NAViEPI
₁₄₈ with five shots per diffusion encoding. This protocol was compared against
₁₄₉ single-shot EPI (Protocol #4) with the same spatial resolution and acceler-
₁₅₀ ation, such as to demonstrate the sampling efficiency of NAViEPI.

₁₅₁ *2.4. Forward modeling*

₁₅₂ Our proposed acquisition method yields multi-dimensional multi-band
₁₅₃ k -space data $\mathbf{y}_{c,q,s}$, where c, q, s denotes the index of the coil sensitivity
₁₅₄ map, the diffusion encoding, and the shot, respectively. Acquisition modeling
₁₅₅ needs to consider several aspects.

₁₅₆ First, the acquired k -space data \mathbf{y} is mapped from individual shot images
₁₅₇ $\mathbf{x}_{q,s,z}$ via the forward model,

$$\begin{aligned} \mathbf{y}_{c,q,s} &= \mathbf{P}_{q,s} \boldsymbol{\Sigma} \boldsymbol{\Theta}_z \mathbf{F} \mathbf{S}_c \mathbf{x}_{q,s,z} \\ \mathbf{y} &:= \mathbf{E}_1 \mathbf{x} \end{aligned} \quad (2)$$

₁₅₈ Here, the encoding matrix \mathbf{E}_1 comprises a chain of linear operators. Every
₁₅₉ shot image \mathbf{x} is point-wise multiplied by a set of coil sensitivity maps (\mathbf{S}) and
₁₆₀ Fourier transformed (\mathbf{F}). The output is then point-wise multiplied by the
₁₆₁ multi-slice phase map ($\boldsymbol{\Theta}$) with z the slice index in simultaneously excited
₁₆₂ slices. This operator shifts individual slice along the phase-encoding direction
₁₆₃ via varying phase modulation (Breuer et al., 2005). The SMS k -space data

164 is then summed (collapsed, Σ) along the slice dimension and masked (point-
165 wise multiplied, \mathbf{P}) by the sampling pattern of each diffusion encoding and
166 shot.

167 Second, for diffusion MRI based on multi-shot EPI, multiple shots ac-
168 quired for a given diffusion encoding need to be combined as one DW image
169 ($\tilde{\mathbf{x}}$). One possibility is to perform magnitude average (Chen et al., 2013)
170 or root-sum-squares (RSS) (Mani et al., 2017) of shot images. This method
171 is robust to in-plane motion, but sub-optimal concerning SNR (Guhaniyogi
172 et al., 2016). Alternatively, shot combination can be done via shot-to-shot
173 phase variation correction (Liu et al., 2005; Chen et al., 2013). This can be
174 incorporated into our formulation as point-wise multiplication between the
175 shot-to-shot phase variation (Φ) and the DW image ($\tilde{\mathbf{x}}$),

$$\mathbf{x}_{q,s,z} = \Phi_{q,s,z} \tilde{\mathbf{x}}_{q,z} \quad (3)$$

176 Note that $\tilde{\mathbf{x}}$ can be obtained by applying the adjoint of Φ to \mathbf{x} . In MUSE,
177 Φ is obtained by parallel imaging reconstruction of all shots with subsequent
178 phase smoothing of every shot image. Based on this phase correction, the
179 complete forward model follows

$$\mathbf{y} := \mathbf{E}_2 \tilde{\mathbf{x}} = \mathbf{E}_1 \Phi \tilde{\mathbf{x}} \quad (4)$$

180 where the encoding matrix \mathbf{E}_2 comprises the chain of the shot-to-shot phase
181 variation Φ and the encoding matrix \mathbf{E}_1 . We implemented these two encoding
182 operators in SigPy (Ong and Lustig, 2019).

183 2.5. Joint k - q -slice reconstruction

184 Based on the generalized forward models in Eqs. (2) and (4), our proposed
185 joint k - q -slice reconstruction can be formulated as a three-step approach.

186 **I. Navigator echo reconstruction.** The acquisition of navigator echoes
 187 follows the forward model in Eq. (2), so the reconstruction of navigator
 188 echoes can be formulated as:

$$\operatorname{argmin}_{\mathbf{x}} \|\mathbf{y} - \mathbf{E}_1 \mathbf{x}\|_2^2 + \lambda \mathbf{R}(\mathbf{x}) \quad (5)$$

189 where $\mathbf{R}(\mathbf{x})$ denotes the regularization functional with the regularization
 190 strength λ . In this work, ℓ^2 regularization was used, i.e., $\mathbf{R}(\mathbf{x}) =$
 191 $\|\mathbf{x}\|_2^2$. In the case of self-navigating (i.e., no navigator acquired) as Pro-
 192 tocol #2, the central k -space region (i.e., 1/4 of the full image matrix)
 193 of each segment is used as \mathbf{y} in Eq. (5).

194 **II. Phase smoothing.** Shot-to-shot phase variation was extracted from
 195 the reconstructed navigator echo phases. Assuming that phase images
 196 are spatially smooth (Chen et al., 2013; Dai et al., 2023), we employed
 197 the adaptive Hanning filter to smooth shot phases,

$$\mathbf{x} = \mathbf{F}^{-1} \mathcal{H}^K \mathbf{F} \mathbf{x} \quad (6)$$

198 where x is the reconstructed navigator image from Step I. \mathcal{H} is the
 199 Hanning window with the non-negative integer K . K controls the width
 200 of the Hanning window.

201 **III. Shot-combined reconstruction.** Joint reconstruction of all DW im-
 202 ages using the shot-combined forward model \mathbf{E}_2 with shot-to-shot phase
 203 variation from Step II reads:

$$\operatorname{argmin}_{\tilde{\mathbf{x}}} \|\mathbf{y} - \mathbf{E}_2 \tilde{\mathbf{x}}\|_2^2 + \lambda \|\mathbf{T}(\tilde{\mathbf{x}})\|_* \quad (7)$$

204 Here, LLR regularization was employed in the local spatial-diffusion
 205 matrices, based on the theory of partially separable functions (Liang,

206 207; Trzasko and Manduca, 2011; Zhang et al., 2015). \mathbf{T} represents
207 a linear operator that firstly slides a local patch window through all
208 DW images and then flattens every set of local patches to construct
209 two-dimensional (2D) spatial-diffusion matrices. The spatial dimension
210 equals the block size, and the diffusion dimension is the number of dif-
211 fusion encodings. $\|\mathbf{T}(\tilde{\mathbf{x}})\|_*$ is the nuclear norm, i.e. the sum of singular
212 values of a spatial-diffusion matrix. This nuclear norm regularization
213 was accomplished via singular value thresholding (SVT) of each spatial-
214 diffusion matrix (Cai et al., 2010). After SVT, the adjoint of \mathbf{T} , \mathbf{T}^H ,
215 was needed to reorder pixel values from the spatial-diffusion matrices
216 back to DW images.

217 To alleviate checkerboard artifacts induced by LLR regularization with
218 non-overlapping blocks (Hu et al., 2020), we employed overlapping blocks.
219 In this case, values from overlapping positions are summed up to the
220 output of \mathbf{T}^H . To enable the correct use of \mathbf{T}^H , we element-wise divided
221 the output of \mathbf{T}^H by a scaling matrix. This matrix was obtained via
222 $\mathbf{T}^H(\mathbf{T}(\mathbf{1}))$, where $\mathbf{1}$ denotes the matrix of all ones with the same shape
223 as the input \mathbf{x} .

224 As the local patch window varies depending on the number of diffusion R1071.9
225 encodings or user selection, we implemented a singular-value spectrum
226 normalization strategy to reduce the effect of the local patch window
227 variation on regularization strength. Specifically, the singular values of
228 constructed spatial-diffusion matrices were divided by the patch win-
229 dow width. After SVT, the thresholded singular values were multiplied
230 with the patch window width for rescaling.

231 2.6. Reconstruction

232 The acquired raw data was read in by twixtools (<https://github.com/pehses/twixtools>). Ramp-sampling regridding and FOV/2-ghost correction were also performed in twixtools. Subsequently, coil sensitivity maps were computed from reference scans using ESPIRiT (Uecker et al., 2014) in SigPy (Ong and Lustig, 2019).

237 With this pre-processing as well as the implemented forward models and proximal operator, the inverse problem in Eq. (7) was solved by the alternating direction method of multipliers (ADMM) (Boyd et al., 2010).

240 ADMM solves the minimization problems in an alternating update scheme,

$$\begin{cases} \mathbf{x}^{(k+1)} := \underset{\mathbf{x}}{\operatorname{argmin}} \| \mathbf{y} - \mathbf{E}(\mathbf{x}) \|^2 + \rho/2 \| \mathbf{T}\mathbf{x} - \mathbf{z}^{(k)} + \mathbf{u}^{(k)} \|_2^2 \\ \mathbf{z}^{(k+1)} := \mathcal{T}_{\lambda/\rho}(\mathbf{T}\mathbf{x}^{(k+1)} + \mathbf{u}^{(k)}) \\ \mathbf{u}^{(k+1)} := \mathbf{u}^{(k)} + \mathbf{T}\mathbf{x}^{(k+1)} - \mathbf{z}^{(k+1)} \end{cases} \quad (8)$$

241 where k denotes the ADMM iteration. \mathbf{z} is the auxiliary variable ($\mathbf{z} = \mathbf{T}\mathbf{x}$), and \mathbf{u} is the Lagrangian multipliers. Importantly, when solving Eq. (2), \mathbf{x} denotes shot images and \mathbf{E} denotes \mathbf{E}_1 in Eq. (8). In contrast, \mathbf{x} denotes shot-combined images and \mathbf{E} denotes \mathbf{E}_2 when solving Eq. (4). \mathbf{x} can be solved using linear least square algorithms, e.g. conjugate gradients (Hestenes and Stiefel, 1952), while \mathbf{z} is updated via singular value thresholding (\mathcal{T}) with the thresholding parameter λ/ρ . The coupling parameter ρ is effective in both the update of \mathbf{x} and \mathbf{z} . It acts as Tikhonov regularization strength when updating \mathbf{x} , but also inversely scales the thresholding strength when updating \mathbf{z} .

251 In this work, 15 ADMM iterations with $\rho = 0.05$ and $\lambda = 0.01$ were used.

252 All reconstructions were done on a single A100 SXM4/NVLink GPU with
253 40 GB memory (NVIDIA, Santa Clara, CA, USA).

254 We compared our proposed joint reconstruction with established multi-
255 shot reconstruction techniques, specifically, MUSE (Chen et al., 2013) and
256 JULEP (Dai et al., 2023), hosted on GitHub by Dr. Dai (Dai et al., 2023).
257 Further, we performed the local-PCA denoising (Cordero-Grande et al., 2019)
258 as implemented in MRtrix (Tournier et al., 2019) on the MUSE reconstructed
259 complex DW images.

260 The in vivo data acquired from Protocol #2 in Table 1 consisted of 126
261 diffusion directions, which exceeds the available GPU memory. Therefore,
262 the 126 data volumes were uniformly split into three parts for our JETS
263 reconstruction with a LLR block width of 6 and the LLR regularization in
264 both Steps I and III in Section 2.5. In addition, MUSE reconstruction was
265 also performed, followed by the local-PCA denoising. Reconstructed DWIs
266 were then processed by DiPy (Garyfallidis et al., 2014) to obtain color-coded
267 fractional anisotropy (cFA) maps.

268 **3. Results**

269 *3.1. Smoothing of shot-to-shot phase variation*

270 Navigators were acquired with the acceleration rate as listed in Table 1.
271 Besides, the base resolution of navigators (e.g. 32 in Protocol #3 in Table 1)
272 was smaller than imaging echoes. As a result, reconstructed navigator phases
273 (refer to the first column in Fig. 3) from Step I in Section 2.5 are not spatially
274 smooth. Such phases, when used in the shot-combined reconstruction, result
275 in signal void artifacts in DW images. To address this problem, we utilized
276 the phase smoothing procedure. As shown in Fig. 3, the ripple-like phase
277 artifact disappears at $K = 5$, while retaining the shot-to-shot phase variation.
278 In contrast, a larger K (e.g., $K = 20$) makes the filter too strong and partially
279 removes phase variation.

R1071.12

280 *3.2. Comparison to MUSE and JULEP with four-shot iEPI acquisition*

281 The iterative phase smoothing was also applicable to MUSE-type self-
282 navigating reconstruction, where shot phases were reconstructed from imag-
283 ing echoes. Fig. 4 compares our proposed JETS with MUSE (Chen et al.,
284 2013), MUSE with complex-valued local-PCA denoiser (Cordero-Grande et al.,
285 2019), and JULEP (Dai et al., 2023). The residual noise from MUSE can be
286 largely removed by the denoiser. However, when compared to JETS, the de-
287 noiser shows residual noise patterns within the globus pallidus (indicated by
288 the red arrow). JETS also shows better denoising than JULEP. The reason
289 is that JETS enforces spatial-diffusion regularization, whereas JULEP for-
290 mulates structured low-rank regularization of the four shots for one diffusion
291 encoding.

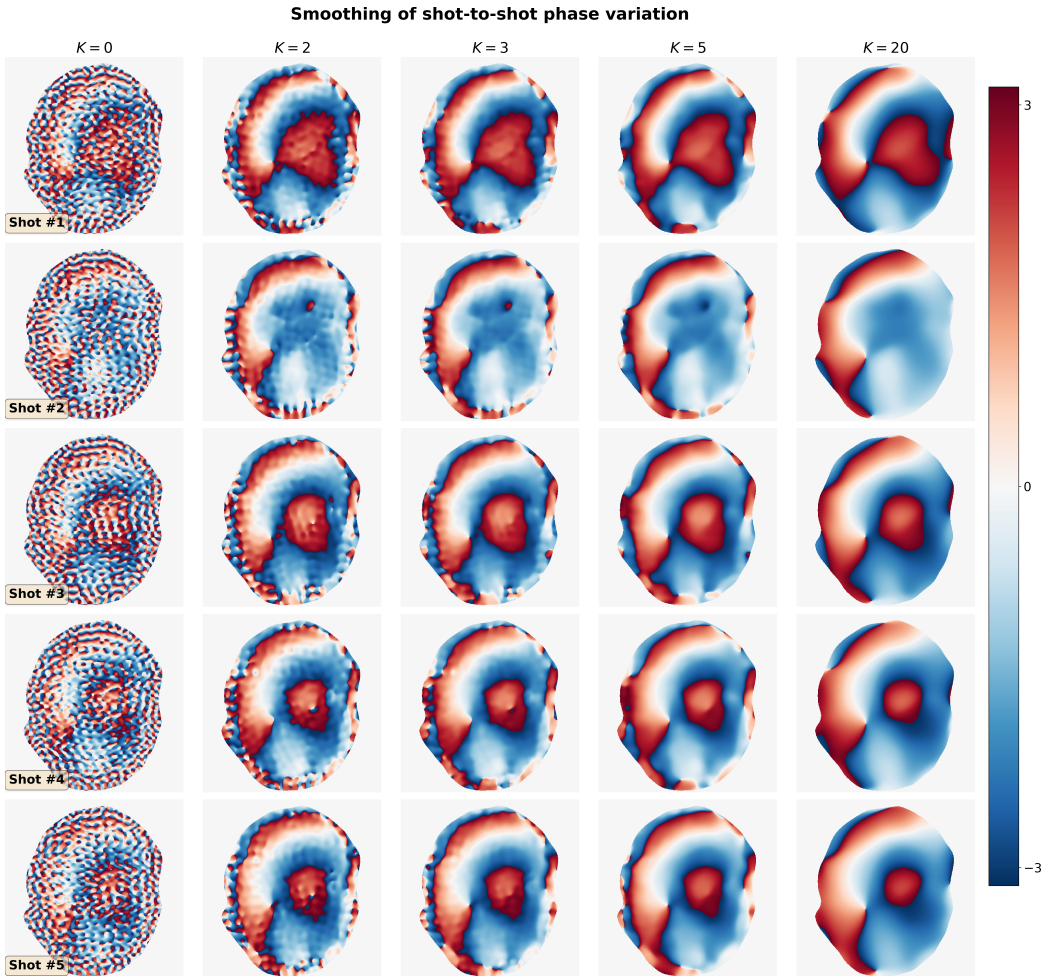


Figure 3: Smoothing of shot-to-shot phase variation according to Eq. (6). Navigators from Protocol #3 were reconstructed based on Step I in Section 2.5 and then used as the input (the column with $K = 0$).

8th DW image from 4-shot iEPI @ 1 mm ISO

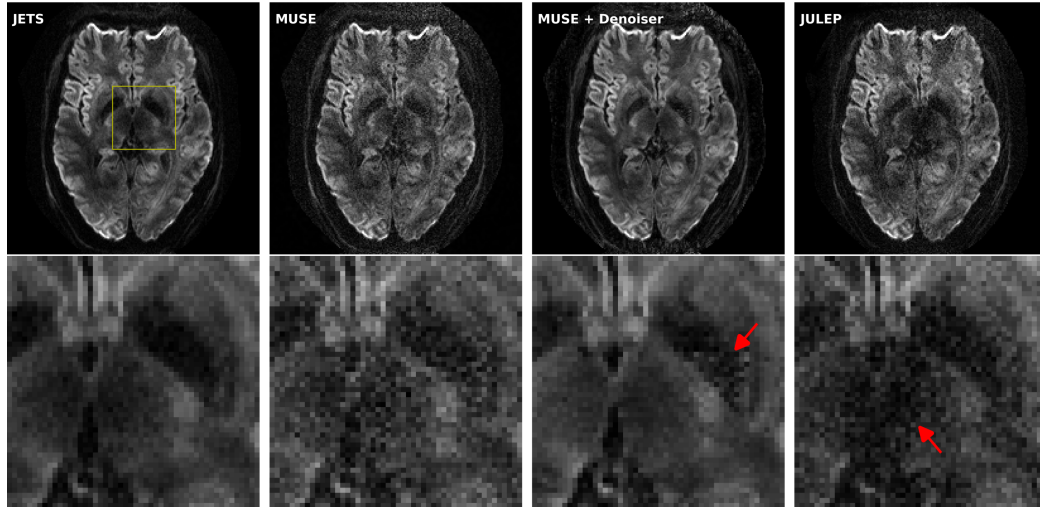


Figure 4: Reconstructed DW images (the 8th diffusion encoding) based on 4-shot iEPI acquisition with 1 mm isotropic resolution (Protocol #1 in Table 1). Four reconstruction methods are compared (from left to right): JETS, MUSE, MUSE with denoiser, and JULEP. The 2nd row displays the magnified views of the yellow square. The image from the denoiser (3rd column) shows residual noise patterns within the globus pallidus (indicated by the red arrow). The JULEP reconstruction (4th column) shows signal dropout in the central region (indicated by the red arrow).

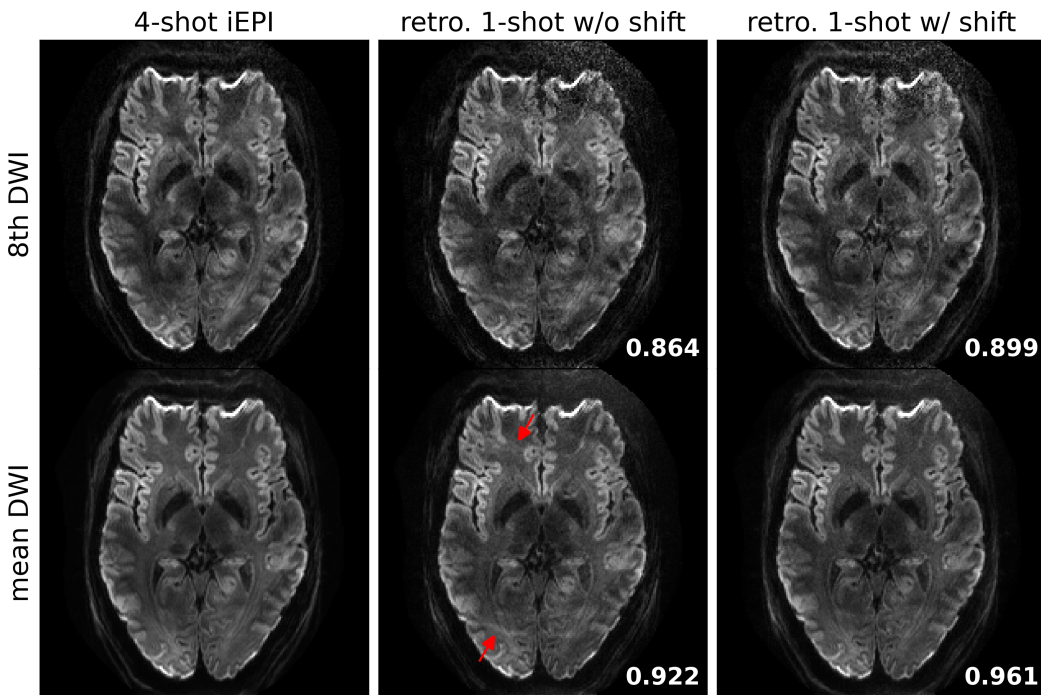


Figure 5: Quantitative validation of the proposed k_y -shift encoding sampling pattern based on 4-shot iEPI acquisition with 1 mm isotropic resolution (Protocol #1 in Table 1). (Top) the 8th diffusion encoding and (bottom) mean DWI over 20 diffusion encodings. (1st column) JETS reconstruction of 4-shot iEPI acquisition is used as the ground truth. The 2nd and the 3rd column displays JETS reconstruction of retrospectively undersampled 1-shot acquisition without and with k_y shifting, respectively. Residual aliasing artifacts are visible in the reconstruction without k_y shifting, as indicated by the red arrows. Structural similarity (SSIM) values are computed and displayed in the bottom right corners.

292 3.3. Retrospectively undersampling from the four-shot iEPI acquisition

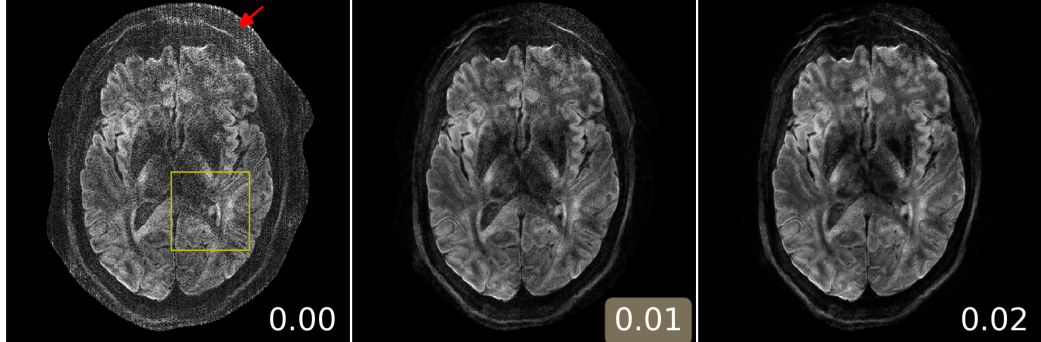
293 JETS reconstruction results on the four-shot prospectively fully-sampled
294 data from Protocol #1 in Table 1, as well as on the retrospectively under-
295 sampled one-shot data without and with the proposed k_y shift are displayed
296 in Fig. 5. Residual aliasing artifacts are visible in the reconstruction with-
297 out k_y shifting, as indicated by the red arrows. In contrast, the k_y shifting
298 scheme supplies a complementary k - q -space sampling pattern, which is bene-
299 ficial for joint reconstructions such as JETS. As shown in Fig. 5, JETS results
300 in improved SSIM values and reduced aliasing artifacts, when compared to
301 the reconstruction without k_y shifting. Figs. 4 and 5 show a slice containing
302 the globus pallidus with strong T_2 -weighted contrast and highlighting the
303 advantage of k_y -shift encoding in reducing undersampling artifacts.

304 3.4. Analysis of reconstruction parameters

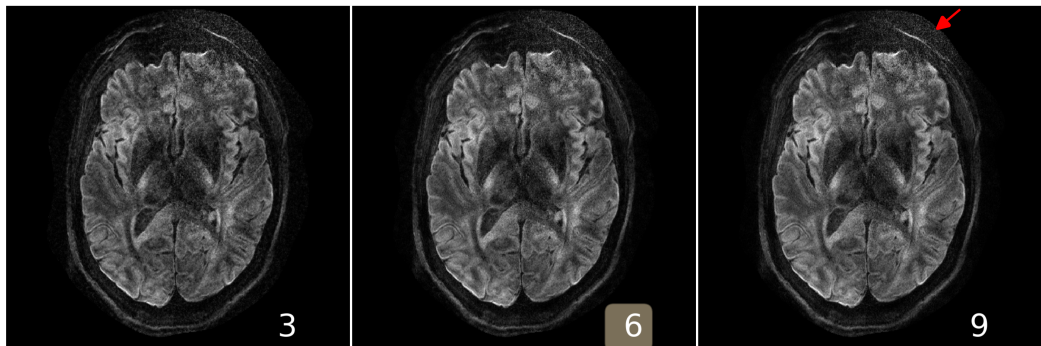
305 Here we provide a systematic analysis of the proposed JETS reconstruc-
306 tion with LLR regularization applied to the spatial-diffusion dimension, as
307 shown in Fig. 6.

308 First, we varied the regularization strength λ . We tested values of 0, 0.08,
309 and 0.16. The reconstruction with $\lambda = 0$ in Eq. (7) corresponds to parallel
310 imaging reconstruction without LLR regularization. It is worth noting that
311 the proposed NAViEPI sequence demonstrates high-quality sub-millimeter
312 DW images ($0.5 \times 0.5 \times 2.0$ mm 3 in this example). The DW images can be
313 further improved with the use of LLR regularization, i.e., reduced noise, as
314 seen in the reconstruction with $\lambda = 0.01$. Increasing λ (e.g. 0.02) further
315 reduces noise, but at the cost of increased blurring. Therefore, $\lambda = 0.01$ was
316 selected in this work.

(A) varying λ , keeping block as 6 and stride as 1



(B) varying block width, keeping λ 0.01 and stride as 1



(C) varying stride, keeping λ as 0.01 and block as 6

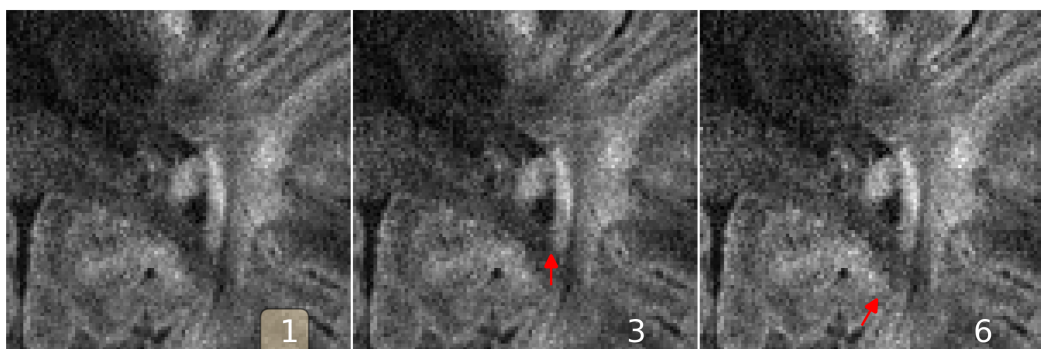


Figure 6: Analysis of reconstruction parameters based on the 3-scan trace acquisition with $0.5 \times 0.5 \times 2.0 \text{ mm}^3$ (Protocol #3 in Table 1). Displayed are JETS reconstructed single-direction DW images. **(A)** Varying the regularization strength λ from 0 to 0.01 and 0.02. **(B)** Varying the block width from 3 to 6 and 9. The red arrow indicates increased noise with the large block width. **(C)** Varying the stride size from 1 to 3 (partially overlapping) and 6 (non-overlapping). The red arrows indicate blocky artifacts.

317 Second, besides the regularization strength, the block size (i.e., the area
318 of 2D patches) also plays a role in denoising. We employed square blocks in
319 this work. Here, the block width of 3 shows the best denoising as compared
320 to 6 and 9, especially in the peripheral brain region.

321 Third, we varied the stride, i.e., the step from one local patch to the
322 next. The use of overlapping LLR (Fig. 6 (C) left) better suppresses blocky
323 artifacts, compared to the partially overlapping (stride < block) LLR (Fig. 6
324 (C) middle) and the non-overlapping (stride = block) LLR (Fig. 6 (C) right).

325 *3.5. Sampling efficiency of NAViEPI*

326 As shown in Fig. 7, NAViEPI achieves sub-millimeter resolution (voxel
327 size $0.5 \times 0.5 \times 2.0 \text{ mm}^3$) with the use of a 5-shot acquisition. When compared
328 to a single-shot acquisition with the same voxel size, the acquisition time of
329 NAViEPI is about two times longer, but the image quality of NAViEPI is
330 remarkably improved.

331 In the sub-millimeter imaging scenario, the increased base resolution re-
332 quires longer TE (143 ms) in the single-shot acquisition, which results in
333 significant signal loss due to T_2 relaxation. Therefore, sub-millimeter DWI
334 necessitates multi-shot acquisition, which is subject to shot-to-shot phase
335 variation and long scan time. However, NAViEPI solves both challenges. The
336 5-shot acquisition reduces TE to 58 ms, and thus retains SNR significantly
337 compared to the single-shot acquisition. Moreover, the JETS reconstruction
338 can help to reduce noise and improve structural visibility.

339 Fig. 8 shows the JETS reconstructed b_0 and TRACE images in different
340 slice locations. Admittedly, the lower brain region (e.g. slice #22) exhibits in-
341 homogeneous and lower signal intensity than the upper slices. Such inhomog-

3-scan trace acquisition with voxel size $0.5 \times 0.5 \times 2.0 \text{ mm}^3$

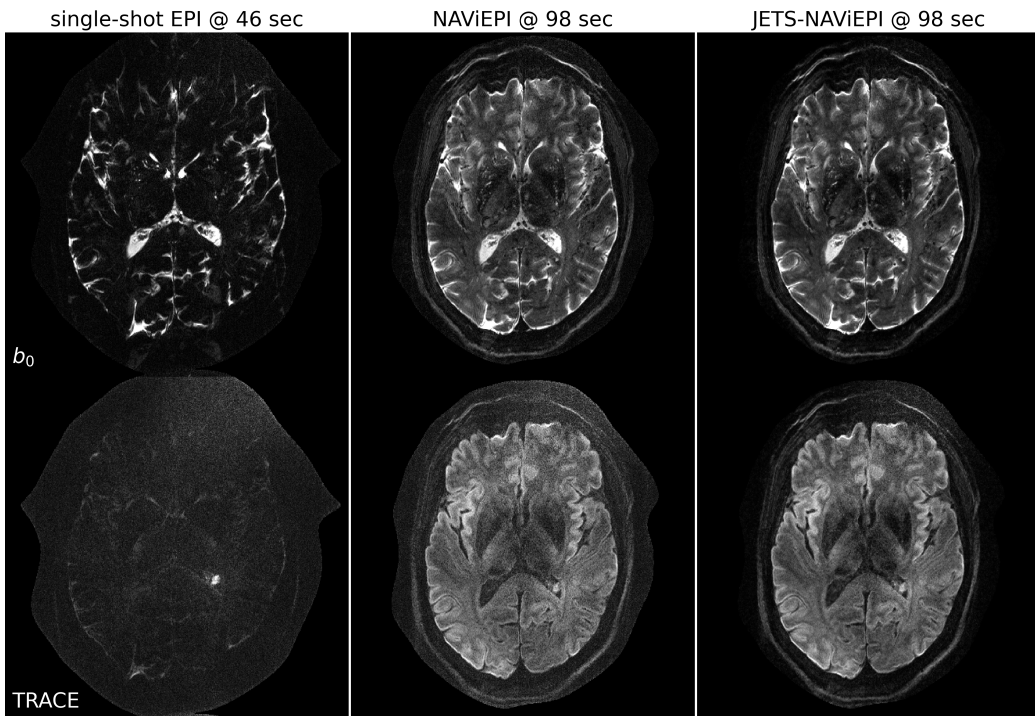


Figure 7: Sampling efficiency of the proposed NAViEPI sequence. 5-shot NAViEPI acquisition with the voxel size $0.5 \times 0.5 \times 2.0 \text{ mm}^3$ (Protocol #3) was compared with single-shot EPI acquisition (Protocol #4). Both the 1st and the 2nd columns were reconstructed via parallel imaging without LLR regularization, whereas the 3rd column was reconstructed via JETS.

3-scan trace acquisition with voxel size $0.5 \times 0.5 \times 2.0 \text{ mm}^3$

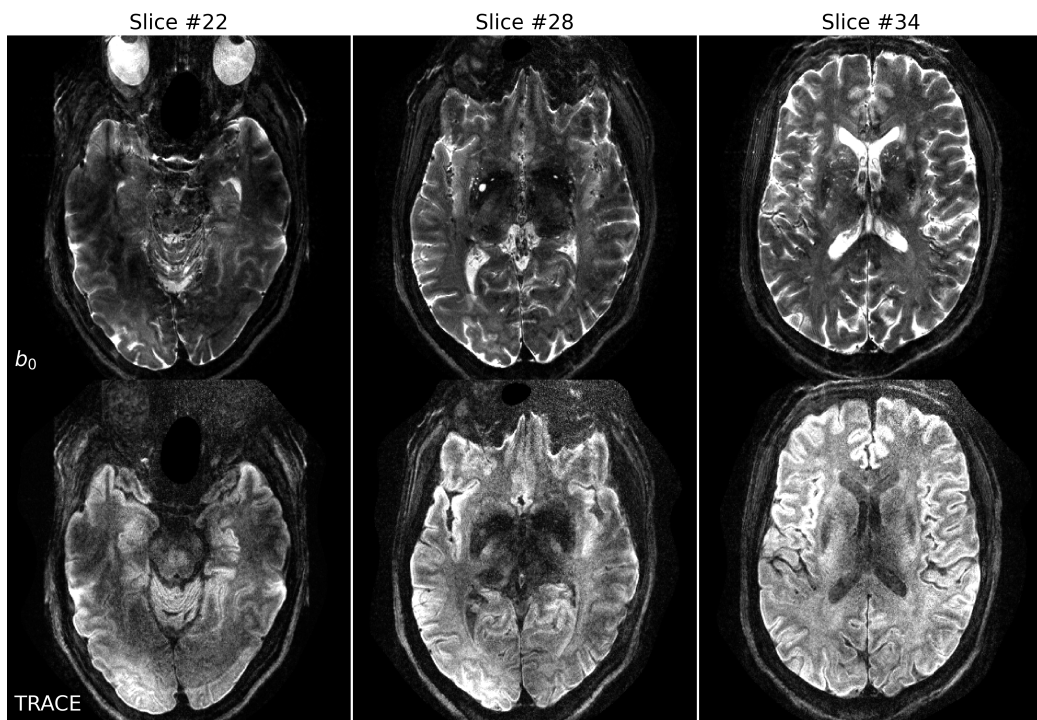


Figure 8: Reconstruction of the 3-scan trace acquisition with the voxel size $0.5 \times 0.5 \times 2.0 \text{ mm}^3$ (Protocol #3) at different slices.

342 geneity can be alleviated with the use of multi-channel parallel transmission
343 (Katscher et al., 2003; Grissom et al., 2010).

344 Here, Figs. 6 and 7 show a slice with a benign lesion (the circular bright R1071.7
345 spot) within the left ventricle. Fig. 8 displays three representative slices:
346 (left) an inferior brain region with marked B_1^+ field inhomogeneity, (mid-
347 dle) the middle brain slice which shows susceptibility artifacts in the frontal
348 region, and (right) a superior brain slice which shows the ventricle.

349 *3.6. Diffusion tensor imaging*

350 Protocol #2 in Table 1 yields an acceleration factor of 6×3 per shot, re-
351 sulting in severe noise amplification in MUSE reconstructed DWIs, as shown
352 in Fig. 9. Here, a slice that highlights the corpus callosum is displayed, and
353 the diffusion direction at the b -value of 3000 s/mm^2 with bright signal within
354 the corpus callosum is shown. The local-PCA denoiser substantially removes
355 noise, but the DWI at high b -values still illustrates more noise, compared to
356 the proposed JETS reconstruction. On the other hand, we applied the local-
357 PCA denoiser before the shot combination in MUSE. As shown in Fig. 9,
358 this approach is less effective compared to the application of the denoiser
359 after the shot combination, because shot images were reconstructed from the
360 central k -space region and have a coarse resolution.

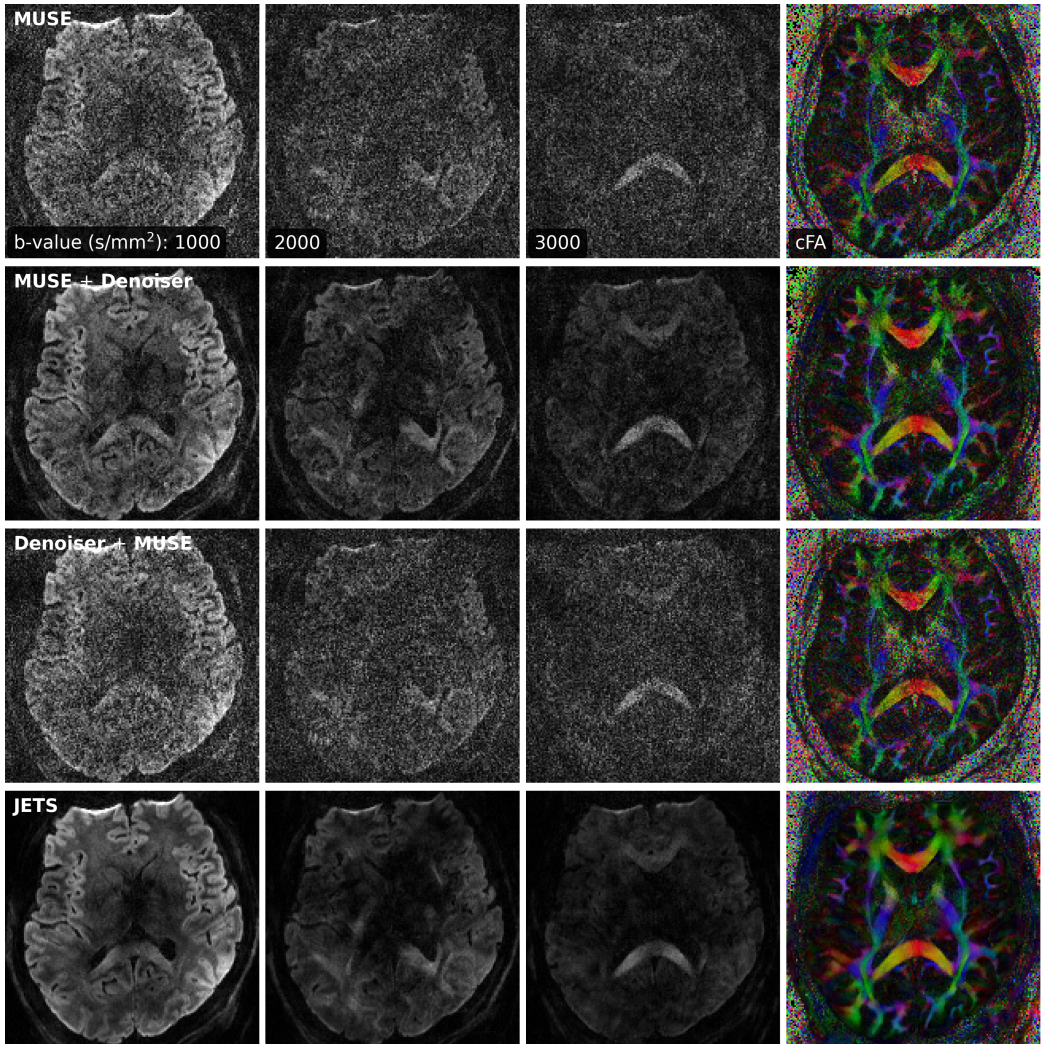


Figure 9: Comparison of three-shell DWIs and cFA maps with data acquired by Protocol #2 in Table 1. Reconstruction methods from top to bottom were MUSE, MUSE with the local-PCA denoiser, the application of the denoiser on shot images before the shot combination in MUSE, and the proposed JETS method.

361 **4. Discussion**

362 This work reports a novel DW-MRI technique, JETS-NAViEPI. NAViEPI
363 (1) achieves the fast and efficient acquisition of both imaging and navigator
364 echoes, (2) enforces consistent effective ESP between the two echoes, and (3)
365 allows for undersampled iEPI as well as a large number of shots. Moreover,
366 compared to the single-shot acquisition, joint k - q -slice reconstruction with k_y -
367 shift encoding on NAViEPI retains SNR and reduces aliasing artifacts in DW
368 images. As a result, JETS-NAViEPI renders high spatiotemporal resolution
369 diffusion MRI protocols in 7 T, e.g., a 3-scan trace acquisition with the voxel
370 size $0.5 \times 0.5 \times 2.0 \text{ mm}^3$ at 1.5 min.

371 One limitation of JETS-NAViEPI is the long reconstruction time due to
372 the simultaneous reconstruction of all DW images and the use of overlapping
373 locally low-rank regularization. The reconstruction for the Protocol #3 in
374 Table 1 on an A100 GPU takes about 2 min per multi-band slice. To reduce
375 the computation time, coil compression algorithms (Buehrer et al., 2007;
376 Huang et al., 2008) can be employed to reduce the number of coils for image
377 reconstruction. Moreover, one can deploy multi-GPU distributed computing
378 or modern optimization algorithms (e.g. stochastic gradient descent) (Ong
379 et al., 2020) to speed up the reconstruction.

380 Neither the signal modeling in Eqs. (2) and (4) nor the LLR regularization
381 considers the subject motion. In the presence of motion, the regularized
382 reconstruction can degrade. To overcome this problem, scout-informed mo-
383 tion estimation and reconstruction (Polak et al., 2022) could be integrated
384 into the framework.

385 Another potential extension of this work is to incorporate distortion cor-

386 rection. The standard distortion correction method is known as TOPUP
387 (Andersson et al., 2003), which acquires two scans with opposing phase-
388 encoding directions to obtain the field inhomogeneity map and then per-
389 forms conjugate phase reconstruction to correct for distortion. Alternatively,
390 a multi-echo acquisition could be used for the coil sensitivity reference scan,
391 such that both coil sensitivity and B_0 field inhomogeneity maps could be
392 reconstructed from the data.

393 This work employed a single regularization weight λ to enforce low rank-
394 ness along the spatial-diffusion direction. However, SNR may be heteroge-
395 neous within the FOV. Therefore, one single regularization scalar may be
396 inadequate to cover the whole FOV. Beyond this SVT-based reconstruction,
397 one can seek to use machine learning to learn a q -space prior as the regularizer
398 (Hammernik et al., 2018; Lam et al., 2019; Mani et al., 2021).

399 Although NAViEPI employs navigators for the acquisition of shot-to-
400 shot phase variation, it is worth noting that phase behavior depends on
401 several hard-to-control factors such as pulsatile motion, bulk motion, loca-
402 tions within the brain, and diffusion sensitization strength. Therefore, more
403 comprehensive modeling or post-processing such as image registration can
404 be considered in future work.

405 This work compared LLR regularized JETS to MUSE post-processed by
406 the local PCA denoiser (Cordero-Grande et al., 2019). Both the LLR regular-
407 ization and the local PCA denoiser are based on the principle that low rank-
408 ness exists in the spatial-diffusion dimension (Moeller et al., 2021), where the
409 spatial content is extracted from local patches within the full image volume
410 and the diffusion dimension is from the q -space encoding. One could integrate

R990.3.b.2

411 the automatic noise estimation based on the Marchenko-Pastur law for the
412 determination of the thresholds in the LLR regularization to synergize these
413 two methods.

414 While this work reconstructs all DW images and then performs model
415 fitting, an alternative approach is to directly estimate b_0 and diffusion ten-
416 sors from measured k - q -space data using model-based reconstruction (Knoll
417 et al., 2015; Dong et al., 2018; Shafieizargar et al., 2023). Compared to DW
418 image reconstruction, model-based reconstruction solves for a fewer number
419 of unknowns, but requires strict diffusion tensor modeling and the use of
420 nonlinear least square solvers.

421 **5. Conclusions**

422 We demonstrated the JETS-NAViEPI technique, which integrates a k_y -
423 shifted encoding navigator-based interleaved EPI sequence and joint recon-
424 struction with overlapping locally low-rank regularization for high spatial-
425 angular-temporal resolution DW-MRI at 7 T. This technique allows for high-
426 quality DW image reconstruction with accelerated acquisitions.

427 **Funding**

428 Funding by the German Research Foundation (DFG) is gratefully ac-
429 knowledged (projects 513220538, 512819079; and project 500888779 of the
430 RU5534 MR biosignatures at UHF). In addition, funding by the National
431 Institutes of Health (NIH), R01 EB024532 and P41 EB017183, is gratefully
432 acknowledged.

433 In addition, we gratefully acknowledge the scientific support and HPC
434 resources provided by the Erlangen National High Performance Computing
435 Center (NHR@FAU) of Friedrich-Alexander-University Erlangen-Nuremberg
436 (FAU) under the NHR project b143dc. NHR funding is provided by federal
437 and Bavarian state authorities. NHR@FAU hardware is partially funded by
438 the German Research Foundation (DFG) – 440719683.

439 **Data and code available statement**

440 In the spirit of reproducible and open science, we publish our source
441 code (<https://github.com/ZhengguoTan/sigpy>) as well as the raw k -space
442 data (<https://doi.org/10.5281/zenodo.7548595>). We also provide inter-
443 active demonstrations of the reconstruction procedure (https://github.com/ZhengguoTan/demo_jets_diffusion_mri_7t).

445 **Acknowledgments**

446 The authors thank Dr. Peter Neher for the discussion on MITK-Diffusion.
447 The authors thank Dr. Berkin Bilgic for making the MUSSELS source code
448 (<https://bit.ly/2QgBg9U>) publically available, Dr. Erpeng Dai for sharing
449 the JULEP source code (<https://github.com/daiep/JULEP>) on GitHub,
450 and Dr. Zhiyong Zhang for sharing the SPA-LLR source code (<https://github.com/ZZgroupSJTU/PMCmsDTI>) on GitHub. The authors also thank
451 Dr. Philipp Ehses for the discussion on twixtools (<https://github.com/pehses/twixtools>).
452

454 **References**

- 455 Andersson, J.L.R., Skare, S., Ashburner, J., 2003. How to correct suscepti-
456 bility distortions in spin-echo echo-planar images: application to diffusion
457 tensor imaging. NeuroImage 20, 870–888. doi:[10.1016/S1053-8119\(03\)00336-7](https://doi.org/10.1016/S1053-8119(03)00336-7).
- 459 Bammer, R., Keeling, S.L., Augustin, M., Pruessmann, K.P., Wolf, R., Stoll-
460 berger, R., Hartung, H.P., Fazekas, F., 2001. Improved diffusion-weighted
461 single-shot echo-planar imaging (EPI) in stroke using sensitivity encoding
462 (SENSE). Magn. Reson. Med. 46, 548–554. doi:[10.1002/mrm.1226](https://doi.org/10.1002/mrm.1226).
- 463 Basser, P.J., Mattiello, J., Le Bihan, D., 1994. MR diffusion tensor
464 spectroscopy and imaging. Biophys. J. 66, 259–267. doi:[10.1016/S0006-3495\(94\)80775-1](https://doi.org/10.1016/S0006-3495(94)80775-1).
- 466 Bilgic, B., Chatnuntawech, I., Manhard, M.K., Tian, Q., Liao, C., Iyer, S.S.,
467 Cauley, S.F., Huang, S.Y., Polimeni, J.R., Wald, L.L., Setsompop, K.,
468 2019. Highly accelerated multishot echo planar imaging through synergistic
469 machine learning and joint reconstruction. Magn. Reson. Med. 82, 1343–
470 1358. doi:[10.1002/mrm.27813](https://doi.org/10.1002/mrm.27813).
- 471 Block, K.T., Uecker, M., Frahm, J., 2007. Undersampled radial MRI with
472 multiple coils. Iterative image reconstruction using a total variation con-
473 straint. Magn. Reson. Med. 57, 1186–1098. doi:[10.1002/mrm.21236](https://doi.org/10.1002/mrm.21236).
- 474 Boyd, S., Parikh, N., Chu, E., Peleato, B., Eckstein, J., 2010. Distributed
475 optimization and statistical learning via the alternating direction method

- 476 of multipliers. Foundations and Trends in Machine Learning 3, 1–122.
477 doi:[10.1561/2200000016](https://doi.org/10.1561/2200000016).
- 478 Breuer, F.A., Blaimer, M., Heidemann, R.M., Mueller, M.F., Griswold, M.A.,
479 Jakob, P.M., 2005. Controlled aliasing in parallel imaging results in higher
480 acceleration (CAPIRINHA) for multi-slice imaging. Magn. Reson. Med.
481 53, 684–691. doi:[10.1002/mrm.20401](https://doi.org/10.1002/mrm.20401).
- 482 Buehrer, M., Pruessmann, K.P., Boesiger, P., Kozerke, S., 2007. Array com-
483 pression for MRI with large coil arrays. Magn. Reson. Med 57, 1131–1139.
484 doi:[10.1002/mrm.21237](https://doi.org/10.1002/mrm.21237).
- 485 Butts, K., Riederer, S.J., Ehman, R.L., Thompson, R.M., Jack, C.R., 1993.
486 Interleaved echo planar imaging on a standard MRI system. Magn. Reson.
487 Med. 31, 67–72. doi:[10.1002/mrm.1910310111](https://doi.org/10.1002/mrm.1910310111).
- 488 Cai, J.F., Candès, E.J., Shen, Z., 2010. A singular value threshold-
489 ing algorithm for matrix completion. SIAM. J. Optim. 20, 1956–1982.
490 doi:[10.1137/080738970](https://doi.org/10.1137/080738970).
- 491 Chen, N.K., Guidon, A., Chang, H.C., Song, A.W., 2013. A robust multi-
492 shot scan strategy for high-resolution diffusion weighted MRI enabled by
493 multiplexed sensitivity-encoding (MUSE). NeuroImage 72, 41–47. doi:[10.1016/j.neuroimage.2013.01.038](https://doi.org/10.1016/j.neuroimage.2013.01.038).
- 495 Cordero-Grande, L., Christiaens, D., Hutter, J., Price, A.N., Hajnal, J.V.,
496 2019. Complex diffusion-weighted image estimation via matrix recovery
497 under general noise models. NeuroImage 200, 391–404. doi:[10.1016/j.neuroimage.2019.06.039](https://doi.org/10.1016/j.neuroimage.2019.06.039).

- 499 Dai, E., Ma, X., Zhang, Z., Yuan, C., Guo, H., 2017. Simultaneous multislice
500 accelerated interleaved EPI DWI using generalized blipped-CAIPI acqui-
501 sition and 3D K-space reconstruction. Magn. Reson. Med. 77, 1593–1605.
502 doi:[10.1002/mrm.26249](https://doi.org/10.1002/mrm.26249).
- 503 Dai, E., Mani, M., McNab, J.A., 2023. Multi-band multi-shot diffu-
504 sion MRI reconstruction with joint usage of structured low-rank con-
505 straints and explicit phase mapping. Magn. Reson. Med. 89, 95–111.
506 doi:[10.1002/mrm.29422](https://doi.org/10.1002/mrm.29422).
- 507 Dai, E., Zhang, Z., Ma, X., Dong, Z., Li, X., Xiong, Y., Yuan, C., Guo, H.,
508 2018. The effects of navigator distortion and noise level on interleaved EPI
509 DWI reconstruction: a comparison between image- and *k*-space method.
510 Magn. Reson. Med. 80, 2024–2032. doi:[10.1002/mrm.27190](https://doi.org/10.1002/mrm.27190).
- 511 Dong, Z., Dai, E., Wang, F., Zhang, Z., Ma, X., Yuan, C., Guo, H., 2018.
512 Model-based reconstruction for simultaneous multislice and parallel imag-
513 ing accelerated multishot diffusion tensor imaging. Med. Phys. 45, 3196–
514 3204. doi:[10.1002/mp.12974](https://doi.org/10.1002/mp.12974).
- 515 Garyfallidis, E., Brett, M., Amirbekian, B., Rokem, A., van der Walt, S.,
516 Descoteaux, M., Nimmo-Smith, I., Contributors, D., 2014. DIPY, a library
517 for the analysis of diffusion MRI data. Front. Neuroinform. 8, 1–17. doi:[10.3389/fninf.2014.00008](https://doi.org/10.3389/fninf.2014.00008).
- 519 Grissom, W.A., Sacolick, L., Vogel, M.W., 2010. Improving high-field MRI
520 using parallel excitation. Imaging Med. 2, 675–693. doi:[10.2217/IIM.10.62](https://doi.org/10.2217/IIM.10.62).

- 522 Griswold, M.A., Jakob, P.M., Heidemann, R.M., Nittka, M., Jellus, V.,
523 Wang, J., Kiefer, B., Haase, A., 2002. Generalized autocalibrating par-
524 tially parallel acquisitions (GRAPPA). Magn. Reson. Med. 47, 1202–1210.
525 doi:[10.1002/mrm.10171](https://doi.org/10.1002/mrm.10171).
- 526 Guhaniyogi, S., Chu, M.L., Chang, H.C., Song, A.W., Chen, N.K., 2016. Mo-
527 tion immune diffusion imaging using augmented MUSE for high-resolution
528 multi-shot EPI. Magn. Reson. Med. 75, 639–652. doi:[10.1002/mrm.25624](https://doi.org/10.1002/mrm.25624).
- 529 Hammernik, K., Klatzer, T., Kobler, E., Recht, M.P., Sodickson, D.K., Pock,
530 T., Knoll, F., 2018. Learning a variational network for reconstruction of
531 accelerated MRI data. Magn. Reson. Med. 79, 3055–3071. doi:[10.1002/mrm.26977](https://doi.org/10.1002/mrm.26977).
- 533 Heidemann, R.M., Porter, D.A., Anwander, A., Feiweier, T., Heberlein, K.,
534 Knösche, T.R., Turner, R., 2010. Diffusion imaging in humans at 7 T
535 using readout-segmented EPI and GRAPPA. Magn. Reson. Med. 64, 9–
536 14. doi:[10.1002/mrm.22480](https://doi.org/10.1002/mrm.22480).
- 537 Hestenes, M.R., Stiefel, E., 1952. Methods of conjugate gradients for solving
538 linear systems. J. Res. Natl. Bur. Stand. 49, 409–436. doi:[10.6028/jres.049.044](https://doi.org/10.6028/jres.049.044).
- 540 Hu, Y., Wang, X., Tian, Q., Yang, G., Daniel, B., McNab, J., Hargreaves, B.,
541 2020. Multi-shot diffusion-weighted MRI reconstruction with magnitude-
542 based spatial-angular locally low-rank regularization (SPA-LLR). Magn.
543 Reson. Med. 83, 1596–1607. doi:[10.1002/mrm.28025](https://doi.org/10.1002/mrm.28025).

- 544 Huang, F., Vijayakumar, S., Li, Y., Hertel, S., Duensing, G.R., 2008. A soft-
545 ware channel compression technique for faster reconstruction with many
546 channels. *Magn. Reson. Imaging* 26, 133–141. doi:[10.1016/j.mri.2007.04.010](https://doi.org/10.1016/j.mri.2007.04.010).
- 548 Jeong, H.K., Gore, J.C., Anderson, A.W., 2013. High-resolution human
549 diffusion tensor imaging using 2-D navigated multishot SENSE EPI at 7
550 T. *Magn. Reson. Med.* 69, 793–802. doi:[10.1002/mrm.24320](https://doi.org/10.1002/mrm.24320).
- 551 Jones, D.K., 2010. Diffusion MRI: Theory, methods, and applications. Oxford
552 University Press. doi:[10.1093/med/9780195369779.001.0001](https://doi.org/10.1093/med/9780195369779.001.0001).
- 553 Katscher, U., Börnert, P., Leussler, C., van den Brink, J.S., 2003. Transmit
554 SENSE. *Magn. Reson. Med.* 49, 144–150. doi:[10.1002/mrm.10353](https://doi.org/10.1002/mrm.10353).
- 555 Knoll, F., Raya, J.G., Halloran, R.O., Baete, S., Sigmund, E., Bammer, R.,
556 Block, T., Otazo, R., Sodickson, D.K., 2015. A model-based reconstruction
557 for undersampled radial spin-echo DTI with variational penalties on the
558 diffusion tensor. *NMR Biomed* 28, 353–366. doi:[10.1002/nbm.3258](https://doi.org/10.1002/nbm.3258).
- 559 Lam, F., Li, Y., Peng, X., 2019. Constrained magnetic resonance spectro-
560 scopic imaging by learning nonlinear low-dimensional models. *IEEE Trans.*
561 *Med. Imaging* 39, 545–555. doi:[10.1109/TMI.2019.2930586](https://doi.org/10.1109/TMI.2019.2930586).
- 562 Le Bihan, D., Breton, E., Lallemand, D., Grenier, P., Cabanis, E., Laval-
563 Jeantet, M., 1986. MR imaging of intravoxel incoherent motions: appli-
564 cation to diffusion and perfusion in neurologic disorders. *Radiology* 161,
565 401–407. doi:[10.1148/radiology.161.2.3763909](https://doi.org/10.1148/radiology.161.2.3763909).

- 566 Liang, Z.P., 2007. Spatiotemporal imaging with partially separable functions,
567 in: 2007 4th IEEE International Symposium on Biomedical Imaging: From
568 Nano to Macro, pp. 988–991. doi:[10.1109/ISBI.2007.357020](https://doi.org/10.1109/ISBI.2007.357020).
- 569 Liu, C., Moseley, M.E., Bammer, R., 2005. Simultaneous phase cor-
570 rection and SENSE reconstruction for navigated multi-shot DWI with
571 non-Cartesian k -space sampling. Magn. Reson. Med. 54, 1412–1422.
572 doi:[10.1002/mrm.20706](https://doi.org/10.1002/mrm.20706).
- 573 Lustig, M., Donoho, D., Pauly, J.M., 2007. Sparse MRI: The application of
574 compressed sensing for rapid MR imaging. Magn. Reson. Med. 58, 1182–
575 1195. doi:[10.1002/mrm.21391](https://doi.org/10.1002/mrm.21391).
- 576 Mani, M., Jacob, M., Kelley, D., Magnotta, V., 2017. Multi-shot sensitivity-
577 encoded diffusion data recovery using structured low-rank matrix comple-
578 tion (MUSSELS). Magn. Reson. Med. 78, 494–507. doi:[10.1002/mrm.26382](https://doi.org/10.1002/mrm.26382).
- 580 Mani, M., Magnotta, V.A., Jacob, M., 2021. qModeL: A plug-and-play
581 model-based reconstruction for highly accelerated multi-shot diffusion MRI
582 using learned priors. Magn. Reson. Med. 86, 835–851. doi:[10.1002/mrm.28756](https://doi.org/10.1002/mrm.28756).
- 584 Mansfield, P., 1977. Multi-planar image formation using NMR spin echoes.
585 J Phys C 10, 55–58. doi:[10.1088/0022-3719/10/3/004](https://doi.org/10.1088/0022-3719/10/3/004).
- 586 Maudsley, A.A., 1980. Multiple-line-scanning spin density imaging. J. Magn.
587 Reson. 41, 112–126. doi:[10.1016/0022-2364\(80\)90207-3](https://doi.org/10.1016/0022-2364(80)90207-3).

- 588 Merboldt, K.D., Hanicke, W., Frahm, J., 1985. Self-diffusion NMR imaging using stimulated echoes. *J. Magn. Reson.* 64, 479–486. doi:[10.1016/0022-2364\(85\)90111-8](https://doi.org/10.1016/0022-2364(85)90111-8).
- 591 Moeller, S., Pisharady, P.K., Ramanna, S., Lenglet, C., Wu, X., Dowdle, L., Yacoub, E., Uğurbil, K., Akçakaya, M., 2021. NOise reduction with DIistribution Corrected (NORDIC) PCA in dMRI with complex-valued 593 parameter-free locally low-rank processing. *NeuroImage* 226, 117539. 594 doi:[10.1016/j.neuroimage.2020.117539](https://doi.org/10.1016/j.neuroimage.2020.117539).
- 596 Mori, S., Crain, B.J., Chacko, V.P., Van Zijl, P.C.M., 1999. Three-dimensional tracking of axonal projections in the brain by magnetic 597 resonance imaging. *Ann. Neurol.* 45, 265–269. doi:[10.1002/1531-8249\(199902\)45:2<265::AID-ANA21>3.0.CO;2-3](https://doi.org/10.1002/1531-8249(199902)45:2<265::AID-ANA21>3.0.CO;2-3).
- 600 Ong, F., Lustig, M., 2019. SigPy: A Python package for high performance 601 iterative reconstruction, in: Proceedings of the 27th Annual Meeting of 602 ISMRM, Montréal, CAN, p. 4819. doi:[10.5281/zenodo.5893788](https://doi.org/10.5281/zenodo.5893788).
- 603 Ong, F., Zhu, X., Cheng, J.Y., Johnson, K.M., Larson, P.E.Z., Vasanawala, 604 S.S., Lustig, M., 2020. Extreme MRI: Large-scale volumetric dynamic 605 imaging from continuous non-gated acquisitions. *Magn. Reson. Med.* 84, 606 1763–1780. doi:[10.1002/mrm.28235](https://doi.org/10.1002/mrm.28235).
- 607 Pipe, J.G., Farthing, V.G., Forbes, K.P., 2002. Multishot diffusion-weighted 608 FSE using PROPELLER MRI. *Magn. Reson. Med.* 47, 42–52. doi:[10.1002/mrm.10014](https://doi.org/10.1002/mrm.10014).

- 610 Polak, D., Splitthoff, D.N., Clifford, B., Lo, W.C., Huang, S.Y., Conklin, J.,
611 Wald, L.L., Setsompop, K., Cauley, S., 2022. Scout accelerated motion
612 estimation and reduction (SAMER). Magn. Reson. Med. 87, 163–178.
613 doi:[10.1002/mrm.28971](https://doi.org/10.1002/mrm.28971).
- 614 Porter, D.A., Heidemann, R.M., 2009. High resolution diffusion-weighted
615 imaging using readout-segmented echo-planar imaging, parallel imaging
616 and a two-dimensional navigator-based reacquisition. Magn. Reson. Med.
617 62, 468–475. doi:[10.1002/mrm.22024](https://doi.org/10.1002/mrm.22024).
- 618 Pruessmann, K.P., Weiger, M., Scheidegger, M.B., Boesiger, P., 1999.
619 SENSE: Sensitivity encoding for fast MRI. Magn. Reson. Med. 42, 952–
620 962. doi:[10.1002/\(SICI\)1522-2594\(199911\)42:5<952::AID-MRM16>3.0.CO;2-S](https://doi.org/10.1002/(SICI)1522-2594(199911)42:5<952::AID-MRM16>3.0.CO;2-S).
- 621
- 622 Ra, J.B., Rim, C.Y., 1993. Fast imaging using subencoding data sets from
623 multiple detectors. Magn. Reson. Med. 30, 142–145. doi:[10.1002/mrm.1910300123](https://doi.org/10.1002/mrm.1910300123).
- 624
- 625 Roemer, P.B., Edelstein, W.A., Hayes, C.E., Souza, S.P., Mueller, O.M.,
626 1990. The NMR phased array. Magn. Reson. Med. 16, 192–225. doi:[10.1002/mrm.1910160203](https://doi.org/10.1002/mrm.1910160203).
- 627
- 628 Setsompop, K., Fan, Q., Stockmann, J., Bilgic, B., Huang, S., Cauley, S.F.,
629 Nummenmaa, A., Wang, F., Rathi, Y., Witzel, T., Wald, L.L., 2018. High-
630 resolution *in vivo* diffusion imaging of the human brain with generalized
631 slice dithered enhanced resolution: Simultaneous multislice (gSlider-SMS).
632 Magn. Reson. Med. 79, 141–151. doi:[10.1002/mrm.26653](https://doi.org/10.1002/mrm.26653).

- 633 Setsompop, K., Gagoski, B.A., Polimeni, J.R., Witzel, T., Wedeen, V.J.,
634 Wald, L.L., 2012. Blipped-controlled aliasing in parallel imaging for si-
635 multaneous multislice echo planar imaging with reduced *g*-factor penalty.
636 Magn. Reson. Med. 67, 1210–1224. doi:[10.1002/mrm.23097](https://doi.org/10.1002/mrm.23097).
- 637 Shafieizargar, B., Jeurissen, B., Poot, D.H.J., Klein, S., Van Audekerke,
638 J., Verhoye, M., den Dekker, A.J., Sijbers, J., 2023. ADEPT: Accurate
639 diffusion echo-planar imaging with multi-contrast shTs. Magn. Reson.
640 Med. 89, 396–410. doi:[10.1002/mrm.29398](https://doi.org/10.1002/mrm.29398).
- 641 Tournier, J.D., Smith, R., Raffelt, D., Tabbara, R., Dhollander, T., Pietsch,
642 M., Christiaens, D., Jeurissen, B., Yeh, C.H., Connelly, A., 2019. MRtrix3:
643 A fast, flexible and open software framework for medical image processing
644 and visualisation. NeuroImage 202, 116137. doi:<https://doi.org/10.1016/j.neuroimage.2019.116137>.
- 645 Trzasko, J., Manduca, A., 2011. Local versus global low-rank promotion in
646 dynamic MRI series reconstruction, in: Proceedings of the 19th Annual
647 Meeting of ISMRM, Montréal, CAN, p. 4371.
- 648 Tuch, D.S., Reese, T.G., Wiegell, M.R., Makris, N., Belliveau, J.W., Wedeen,
649 V.J., 2002. High angular resolution diffusion imaging reveals intravoxel
650 white matter fiber heterogeneity. Magn. Reson. Med. 48, 577–582. doi:[10.1002/mrm.10268](https://doi.org/10.1002/mrm.10268).
- 651 Uecker, M., Lai, P., Murphy, M.J., Virtue, P., Elad, M., Pauly, J.M.,
652 Vasanawala, S.S., Lustig, M., 2014. ESPIRiT – an eigenvalue approach

- 655 to autocalibrating parallel MRI: Where SENSE meets GRAPPA. Magn.
656 Reson. Med. 71, 990–1001. doi:[10.1002/mrm.24751](https://doi.org/10.1002/mrm.24751).
- 657 Wu, W., Koopmans, P.J., Andersson, J.L., Miller, K.L., 2019. Diffusion
658 Acceleration with Gaussian process Estimated Reconstruction (DAGER).
659 Magn. Reson. Med. 82, 107–125. doi:[10.1002/mrm.27699](https://doi.org/10.1002/mrm.27699).
- 660 Wu, W., Miller, K.L., 2017. Image formation in diffusion MRI: A review
661 of recent technical developments. J. Magn. Reson. Imaging 46, 646–662.
662 doi:[10.1002/jmri.25664](https://doi.org/10.1002/jmri.25664).
- 663 Zhang, T., Pauly, J.M., Levesque, I.R., 2015. Accelerated parameter mapping
664 with a locally low rank constraint. Magn. Reson. Med. 73, 655–661. doi:[10.1002/mrm.25161](https://doi.org/10.1002/mrm.25161).